Fault-Slip Source Models for the 2011 M 7.1 Van Earthquake in Turkey from SAR Interferometry, Pixel Offset Tracking, GPS, and Seismic Waveform Analysis

by Eric J. Fielding, Paul R. Lundgren, Tuncay Taymaz, Seda Yolsal-Çevikbilen, and Susan E. Owen

Online Material: Additional point-source mechanisms for mainshock/aftershocks listed in table 2; snapshots, movie of bodywave finite-fault model; additional information on source modeling.

INTRODUCTION

A large M_w 7.1 earthquake struck the area north of the city of Van in easternmost Turkey on 23 October 2011. The mainshock epicenter and most of the aftershocks were located south of the eastern arm of Lake Van (Fig. 1), and extensive damage was reported in the city of Van, the city of Erciş, and many smaller towns nearby. The Lake Van region has suffered from a large number of historical earthquakes, with many causing significant damage in the last 2000 years (Table 1; Ergin *et al.*, 1967; Ambraseys and Jackson, 1998; Albini *et al.*, 2012). The region is near the center of the elevated Turkish–Iranian Plateau (also called the Anatolian Plateau) in the collision zone between the Arabian and Eurasian plates, and is well to the east of the escape tectonics exhibited along the major strike-slip North Anatolian and East Anatolian faults (e.g., Jackson and McKenzie, 1984; Taymaz *et al.*, 1991, 2007; Yolsal-Çevikbilen *et al.*, 2012). The plateau has an average elevation around 2000 m (Copley and Jackson, 2006; Tan and Taymaz, 2006; Podgorski *et al.*, 2007), and Lake Van has an elevation of about 1650 m above sea level. The Moho depth in the Van area, inferred from receiver-function and surface-wave analysis, is approximately 43 km, in the middle of a Moho gradient from about 40 km in the south to 50 km under the Pontides Mountains at the northern edge of the plateau (Gök *et al.*, 2011; Vanacore *et al.*, 2013). There are many Quaternary mafic volcanoes in the area (Fig. 1), which likely result from elevated temperatures in the upper mantle and possible delamination of part of the subducted Arabian lithosphere (Şengör *et al.*, 2003; Maggi and Priestley, 2005; Barazangi *et al.*, 2006; Gök *et al.*, 2011). The uppermost mantle has extremely low seismic velocities (Zor *et al.*, 2003; Bakırcı *et al.*, 2012) and blockage of S_n propagation (Gök *et al.*, 2003; Al-Damegh *et al.*, 2004), indicating the complete lack of a mantle lid (Barazangi *et al.*, 2006).

Geodetic studies with Global Positioning System (GPS) data measure the northward motion of the Arabian plate relative to Eurasia at about 18 mm/year in eastern Turkey (Reilinger *et al.*, 2006). The GPS data also show ongoing north–south compressional strain within this area of the Turkish–Iranian Plateau. Several authors have interpreted systems of strike-slip faults as absorbing most of this north–south contraction (Jackson and McKenzie, 1984; Taymaz *et al.*, 1991; Koçyiğit *et al.*, 2001; Şengör *et al.*, 2003; Copley and Jackson, 2006). Many of the earthquakes within the plateau that were large enough for focal mechanism analysis showed predominantly strike-slip motion (Jackson and McKenzie, 1988; Jackson *et al.*, 2002; Örgülü *et al.*, 2003; Copley and Jackson, 2006; Tan and Taymaz, 2006), including the large M_w 7.0 Çaldıran–Muradiye earthquake of 24 November 1976, which was about 90 km to the northeast of the 2011 Van earthquake (Fig. 1; Taymaz, 1996).

In this study we compare coseismic source models for the Van earthquake derived from surface deformation measurements and seismic waveform modeling. We analyze geodetic data for the coseismic surface deformation from interferometric synthetic aperture radar (InSAR) and GPS data to constrain finite fault slip models. InSAR data include interferograms from two European Space Agency Envisat Advanced Synthetic Aperture Radar (ASAR) descending-track pairs and one Italian Space Agency COSMO-SkyMed (CSK) descending-track pair, along with pixel-offset tracking (subpixel correlation) along-track displacements from the CSK pair. Continuous GPS data posted to the Group on Earth Observations (GEO) Geohazards Supersite by the Turkish government were analyzed to estimate the three-component station coseismic displacements. We also analyze teleseismic *P*- and *SH*-waveforms to estimate

doi: 10.1785/0220120164

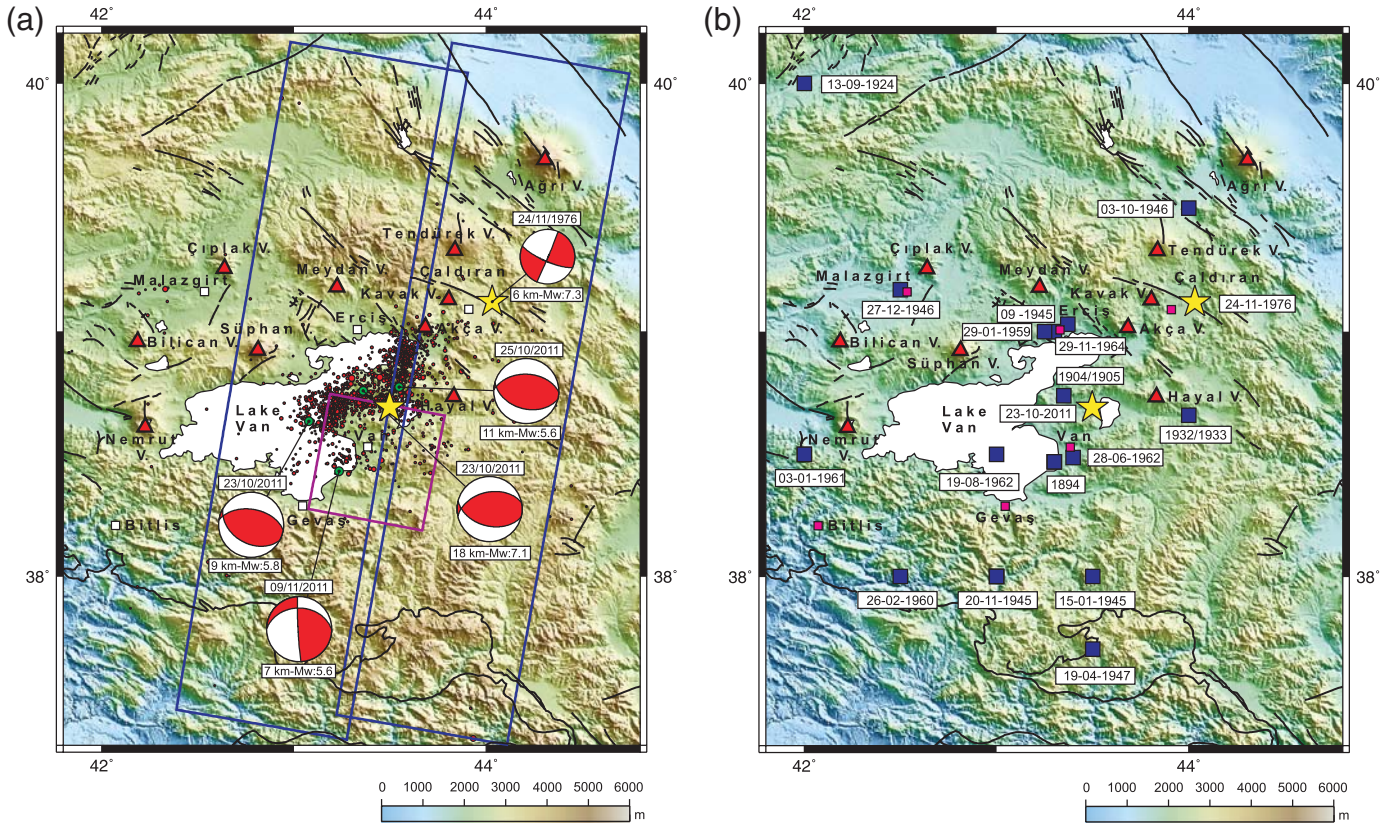

▲ **Figure 1.** (a) Location map; yellow star, 2011 M_w 7.1 Van earthquake mainshock (NEIC location); red circles, aftershock epicenters (KOERI-UDIM) plotted over shaded-relief topography from Global Multi-resolution Terrain Elevation Data 2010 (GMTED2010); dark-blue rectangular outlines, coverage of Envisat images; purple rectangular outlines, CSK SAR images used in the geodetic data analysis; red triangles and pink squares, locations of major volcanoes and cities in the area, respectively; black lines, active faults mapped in the area. Lower hemisphere projections of the focal mechanisms corresponding to the minimum misfit solutions of earthquakes studied here (2011 events; see Table 2 and Ⓔ electronic supplement for details) and by earlier workers (1976 event; Nabelek, 1984; Taymaz, 1996) are also plotted with red compressional quadrants; green circles, KOERI-UDIM locations of 2011 events. Event dates, magnitudes (M_w), and the focal depths (h) obtained from the inversions are shown above and below the focal spheres, respectively. (b) Blue squares marked nearby with dates as dd-mm-yyyy plotted over shaded-relief topography, locations of historical earthquakes since 1894. Other symbols are as in (a); yellow stars, locations of 2011 Van and 1976 M_w 7.3 Çaldıran–Muradiye earthquakes (see bold lines in Table 1).

the source parameters of a point source that best matches the waveforms, and a finite-fault slip distribution that is consistent with the point-source parameters. Finally, we compare the source models to each other and to seismicity and field observations.

SEISMIC WAVEFORM INVERSION

We performed point-source inversions using teleseismic long-period *P*- and *SH*- and broad-band *P* waveforms recorded by the International Federation of Digital Seismograph Networks (FDSN) and the Global Digital Seismograph Network (GDSN) stations (Taymaz, 1993; Tan and Taymaz, 2006; Taymaz *et al.*, 2007; Yolsal-Çevikbilen and Taymaz, 2012) in order to determine source parameters of the 2011 Van earthquake and its aftershocks (Fig. 2). We used the MT5 algorithm of the body-waveform inversion method provided by McCaffrey *et al.* (1991) and Zwick *et al.* (1994). Velocity responses were deconvolved from the records and then we re-convolved them with the response of the old World Wide Standard Seismographic Network (WWSSN) 15–100 s long-period instruments. We compared the shapes and amplitudes of long-period *P* and *SH* and broadband *P* waves recorded in the distance range of 30°–90°. Synthetic waveforms were formed by the combination of direct (*P* or *SH*) and reflected (*pP* and *sP*, or *sS*) phases from a point source embedded in a given velocity structure. We used a half-space source velocity model consisting of *P*-wave velocity (V_p) = 6.8 km/s, *S*-wave velocity (V_S) = 3.9 km/s, and density (ρ) = 2.9 g/cm^3 given by Zwick *et al.* (1994) and Tan and Taymaz (2006), a simplified crustal model for teleseismic waveform modeling with the MT5 algorithm. Receiver structures are assumed to be homogeneous half-spaces. Seismograms were weighted according to the azimuthal distribution of stations.

Table 1
Historical Earthquakes of the Lake Van Region Based on KOERI-UDIM and Kazim Ergin Catalogs

Date (yyyy/mm/dd)	Time (hh:mm:ss.ss)	Latitude (°)	Longitude (°)	Depth (km)	Magnitude	Intensity	Location/Affected Region	Reference*
869		40.00	44.00			IX	At Erivan	KOERI
1101		38.47	43.30			VI	At Van	K.ERGIN
1111		38.47	43.35			IX	At Van/vicinity of Van Lake	K.ERGIN
1276		38.90	42.90			VII	At Ahlat, Erciş, and Van	K.ERGIN
1646–1648		38.47	43.30			VI	At Van region	K.ERGIN
1701		38.47	43.65			VII	At Van	K.ERGIN
1704		38.47	43.65			VI	At Van	K.ERGIN
1715		38.70	43.50			VI	At Van and Erciş region	K.ERGIN
1791		39.00	43.70			VI	At Van, Tebriz, and Erzurum	K.ERGIN
1871/03/5–25		38.47	43.35			VII	At Van region	K.ERGIN
1881/05/30		38.50	43.30			IX	At Van and vicinity Bitlis, Muş	KOERI
1881/06/07		38.47	43.30			VII	At Van and Nemrut region	K.ERGIN
1894		38.47	43.30			V	At Van	K.ERGIN
1900/6,9		38.47	43.30			VI	At Van	K.ERGIN
1902		39.00	43.30			VI	At Erciş	K.ERGIN
1903/04/28	23:46:00.00	39.10	42.50	30	6.3			KOERI
1904/1905		38.74	43.35			VI	At Van region	K.ERGIN
1908/09/28	06:28:00.00	38.00	44.00	30	6.0			KOERI
1924/09/13	14:34:14.70	39.96	41.94	10	6.8			KOERI
1930/05/06	22:34:31.70	37.98	44.48	70	7.6			KOERI
1930/0508	15:35:27.00	37.97	45.00	30	6.3			KOERI
1932–1933		38.66	44.00			VI	At Özalp in Van	K.ERGIN
1935/05/01	10:24:46.30	40.09	43.22	60	6.2			KOERI
1941/09/10	23:53:00.00				5.9	VIII	At Erciş	KOERI
1945/01/15		38.00	43.50			VI	At Van and Muradiye	K.ERGIN
1945/07/29		38.00	43.00			VII	Destruction at Van	K.ERGIN
1945/09		39.00	43.30				At Erciş	K.ERGIN
1945/11/20		38.00	43.00			VIII	At Van	K.ERGIN
1946/10/03		39.50	44.00				Van Lake	K.ERGIN
1946/12/27		39.17	42.50				Vicinity of Van Lake	K.ERGIN
1947/04/19		37.70	43.50				Southeast of Van Lake	K.ERGIN
1959/01/29		39.00	43.25				Vicinity of Van Lake in Turkey	K.ERGIN
1960/02/26		38.00	42.50				South of Van Lake in Turkey	K.ERGIN
1960/09/03		38.50	42.00				Turkey, Van Lake region	K.ERGIN
1961/01/03		38.50	42.00				Turkey, Van Lake region	K.ERGIN
1961/09/04		38.00	43.00				Turkey, Van Lake region	K.ERGIN
1962/06/28		38.49	43.40			IV	Turkey, Van and Özalp	K.ERGIN
1962/08/19		38.50	43.00				Turkey, Van Lake region	K.ERGIN
1964/09/29		39.03	43.37			III	Turkey, at Erciş	K.ERGIN
1966/08/19	12:22:10.50	39.17	41.56	26	6.5			KOERI
1976/11/24	**14:22:15.60**	**39.05**	**44.04**	**10**	**7.5**	**IX**	**At Çaldıran–Muradiye**	**KOERI**
2011/10/23	**10:41:22.93**	**38.69**	**43.49**	**16**	**7.1**		**North of Van city**	**USGS-NEIC**

*K.ERGIN and KOERI events are from (Ergin *et al.*, 1967) and (KOERI-UDIM, 2012), respectively.

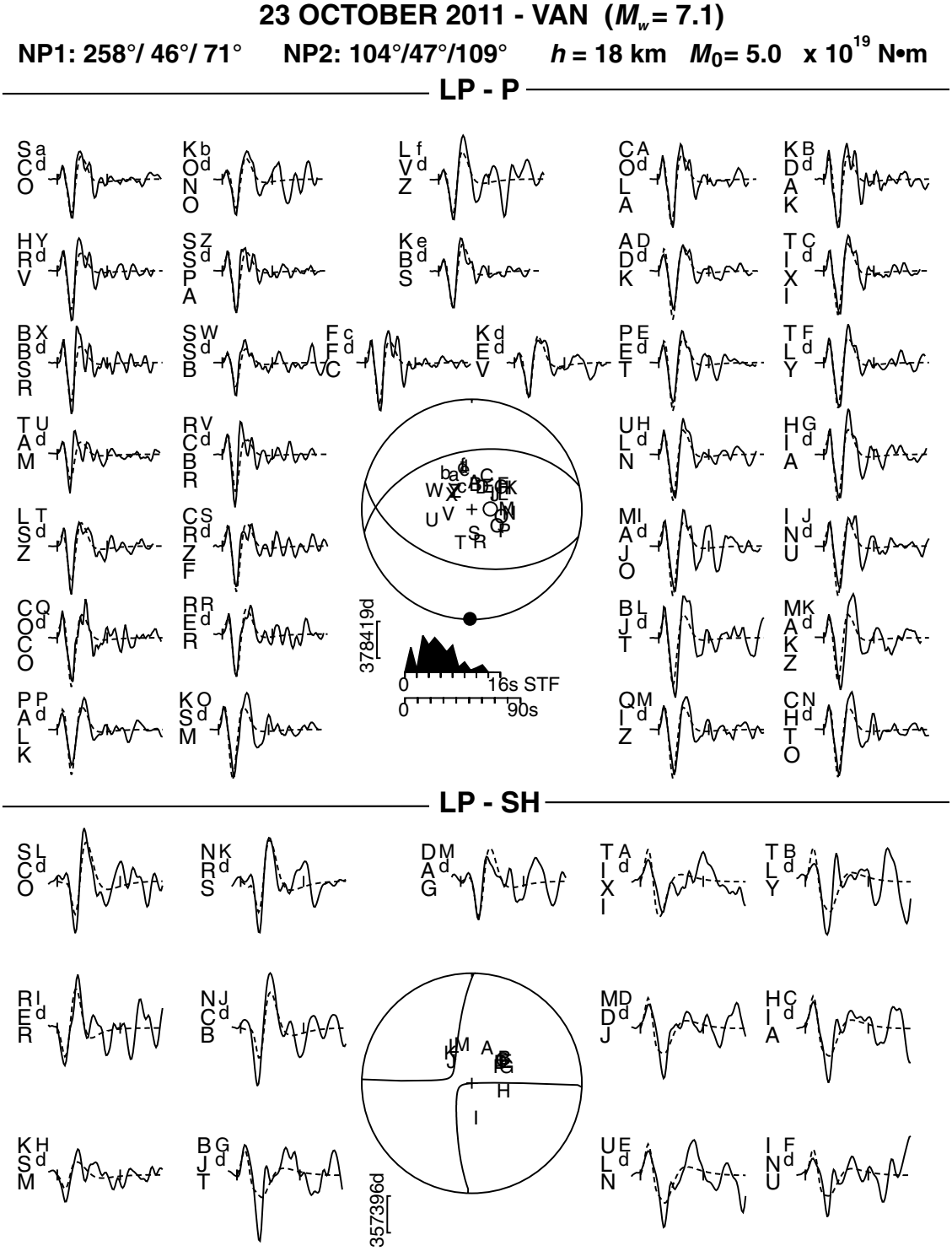

▲ **Figure 2.** The radiation patterns and synthetic waveform fits for the minimum misfit solution obtained from the point-source inversion of the 2011 Van mainshock; dashed lines, fits to all long-period 32 *P*- and solid lines, 13 *SH*-waveforms used in the inversion. Beneath the header at the top of the figure that shows the date and moment magnitude, are given the strike, dip, and rake angles of the first and second nodal planes (NP), focal depth (h), and seismic moment (M_0). The source time function (STF) is shown in the middle of the figure, and beneath it is the time scale used for the waveforms. Focal spheres are shown with *P*- (top) and *SH*- (bottom) nodal planes in lower hemisphere projections. The vertical bar beneath the focal spheres shows the waveform displacement scale in microns, with the lower-case letter identifying the instrument type (d: GDSN long period). Station positions are indicated by letter and are arranged alphabetically clockwise, starting from north. The *P* and *T* axes are marked by solid and open circles, respectively. Total duration of source time function (STF) is 14 s, but most of the moment release occurred in the first 10 s.

We employed the conventional values of 1.0 and 4.0 s for the attenuation parameter (t^*; Futterman, 1962) for 32 *P* and 13 *SH* waves, respectively, $t^* = t/Q$, in which t is travel time and Q is the averaged attenuation along the ray path. These values are within 10% of those estimated for the mantle (e.g., Dziewonski and Anderson, 1981). More precise values of (t^*) cannot be independently determined using the inversion routine because of significant trade-off between (t^*) and the source time function (Nabelek, 1984, 1985; Christensen and Ruff, 1985; Wagner and Langston, 1989). Each of the phases, *pP*, *sP*, *sS*, and *pS* contains as much information about the source as the direct waves. By recognizing these phases it is theoretically possible, in many fault-plane orientations, to find a well-constrained fault-plane solution using very few stations by modeling the *P* and *SH* waveforms and relative amplitudes. Resolution of all source parameters may be degraded, of course, by such factors as poor station distribution, poor signal-to-noise (SNR) ratios or source complexities. Uncertainties in t^* affect mainly source duration and seismic moment, rather than source orientation or focal (centroid) depth (Fredrich *et al.*, 1988).

The point-source inversion routine adjusts the strike (ϕ), dip (δ), and rake (λ) angles of the fault plane, the focal depth (h), scalar seismic moment (M_0), and source time function. The source time function is described by a series of overlapping isosceles triangles for which the number and duration is estimated within the inversion (see Ⓔ supplementary material, available in the electronic supplement to this paper). Having found a set of acceptable point source parameters (strike 258°, dip 46°, rake 71°, depth 18 km, and M_0 5.0×10^{19} N·m; see Fig. 2 and Table 2), we followed the procedure described by Taymaz and Price (1992), Taymaz *et al.* (2007), and Yolsal-Çevikbilen and Taymaz (2012), in which the inversion routine is used to carry out experiments to test how well individual source parameters are resolved. Uncertainty tests show the robustness of the minimum misfit solutions revealing that the error limits of strike, dip, and rake angles are approximately ±5°–10°, and of focal depths is ±2 km. In this case, the slip vector at the hypocenter plunges at 43° toward 14°. The detailed point-source parameters of October 2011 Lake Van earthquake and major aftershocks ($M_w \geq 5.0$) obtained from teleseismic *P*- and *SH*-waveform modeling are listed in Table 2.

Our preferred best-fitting waveform point-source solution (Fig. 2) obtained by using FDSN–GDSN teleseismic stations shows a reverse faulting mechanism with a small strike-slip component. The two nodal planes in this point-source solution dip steeply to the north and south and have a small amount of oblique slip. The along-track (roughly north–south) displacements from the CSK data (described subsequently) show that the area to the south of the epicenter moved southward, which requires that the main rupture dips to the north, so we take the north-dipping plane (strike 258° ± 5°, dip 46° ± 5°, rake 71° ± 5°) as the fault plane, with uncertainties estimated by using the inversion routine to carry out a variety of experiments (Taymaz *et al.*, 2007). The centroid depth is 18 ± 2 km (although this does not include uncertainty related to the simplified velocity structure), and seismic moment M_0 5.0×10^{19} N·m (M_w 7.07) in the preferred waveform fit using a shear modulus of 44 GPa, given by the velocity model (see Fig. 2).

An alternative point-source solution is shown in Ⓔ Figure S1 (see supplement) using broadband *P* waveforms alone. That solution has a seismic moment of 6.88×10^{19} N·m (using the same velocity model), but is less reliable than our preferred solution using the *P* and *SH* waveforms. In Ⓔ Figure S2 (see supplement), we show selected waveform fits for the Global Centroid Moment Tensor (GCMT) Project (www.globalcmt.org/CMTsearch.html; last accessed February 2013), USGS body-wave, USGS *W* phase, and USGS CMT solutions compared with our preferred point-source mechanism. These waveforms were chosen near nodal planes to enhance information about the mechanism, and our preferred point source fits the waveforms better overall. Ⓔ Figures S3–S7 (see supplement) and Table 2 show point-source solutions for three large aftershocks (M_w 5.6 to M_w 5.8) of the M_w 7.1 Van mainshock.

For finite-fault slip distributions, we used an inversion scheme developed by Yoshida (1992) and Yagi and Kikuchi (2000) with the Jeffreys–Bullen velocity-depth model (Jeffreys and Bullen, 1940, 1958; Ⓔ Table S1, see supplement) and FDSN-GDSN teleseismic broadband *P* waveforms were made available through the Data Management Center of the Incorporated Research Institutions for Seismology (IRIS-DMC). At this time, the slip inversion code for the Yagi and Kikuchi (2000) algorithm is less stable when *SH* waveforms are

Table 2
Source Parameters of 23 October 2011 Van Earthquake and Major Aftershocks ($M_w \geq 5.0$) Obtained from Teleseismic *P*- and *SH*-Waveform Modeling (See Fig. 1a)

Date (yyyy/mm/dd)	Origin Time (t_o) (hh:mm:ss)	Latitude (°N)	Longitude (°E)	M_w	Strike (°)	Dip (°)	Rake (°)	*H* (km)	M_0(×10^{17} N·m)
2011/10/23	10:41:22	38.69	43.49	7.1	258±5	46±5	71±5	18±2	500
2011/10/23	20:45:37	38.55	43.16	5.8	279±5	50±5	77±5	9±2	6.31
2011/10/25	14:55:09	38.81	43.62	5.6	272±5	47±5	81±5	11±2	2.86
2011/11/09	19:23:35	38.42	43.22	5.6	271±5	35±5	185±5	7±2	3.26

Earthquake locations are taken from USGS-NEIC earthquake catalog. *H*: centroid depth (km), M_0: seismic moment (N·m; see Ⓔ electronic supplement for details of waveform fits)

included, so we used only the *P* waveforms (Yagi, Nakao, Kasahara, 2012; Yagi, Nishimura, Kasahara, 2012). Teleseismic waveforms were windowed for 60 s, starting 10 s before the origin time (t_0). After band-pass filtering between 0.01 and 0.8 Hz, they were converted into ground displacement with a sampling rate of 0.20 s. A numerical method for the standard waveform inversion scheme given by Hartzell and Heaton (1983) and Yoshida (1992) was used to construct the earthquake source model. We assumed that faulting occurs on a single fault plane, and that rake remains unchanged during the rupture. The rupture process was then presented as a spatio-temporal slip distribution on a fault plane which was divided into $M \times N$ sub-faults with length dx and width dy. Then, the source time function on each sub fault was described by a series of triangle functions with an assumed rise time ($\tau = 1$ s). Green's functions were calculated using the method of Kikuchi and Kanamori (1991). We also applied smoothing constraints to the slip distribution with respect to time and space to prevent instabilities, which may occur as a result of increasing the number of model parameters in the inversions (e.g., Hartzell and Heaton, 1983; Yoshida, 1992; Yoshida *et al.*, 1996; Yagi and Kikuchi, 2000; Taymaz *et al.*, 2007). No constraint was placed on the total moment (see Ⓔ electronic supplement for further details).

The finite-fault model from the inversion of 39 teleseismic broadband *P* waveforms is shown in Figure 3. The fault plane was fixed to the best-fitting point-source solution and was then divided into 8×16 subfaults with dimensions of 5×5 km^2. The source time (slip-rate) function of each subfault is expanded in a series of three overlapping triangle functions each with a rise time (τ) of 1.0 s. The rupture-front velocity (V_r) is 3.2 km/s. Our preferred teleseismic slip model has most of the fault slip close to the hypocenter. As described previously, the rake was constrained to be constant, and the optimum value

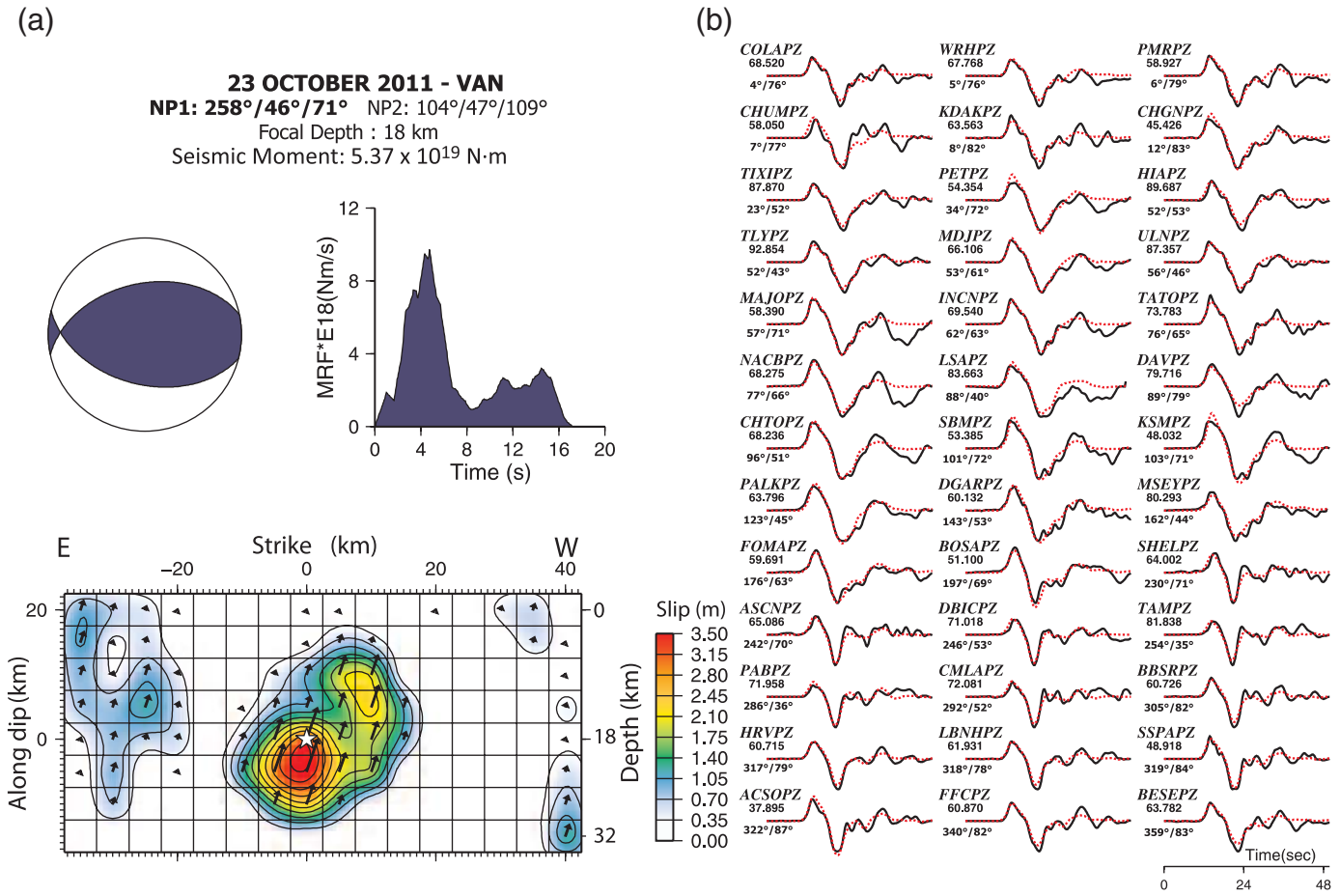

▲ **Figure 3.** (a) Focal mechanism, coseismic slip distribution, and total moment rate function of the 23 October 2011 Van earthquake from teleseismic broadband body-wave finite-fault inversion. The strike, dip, and rake angles of the first and second nodal planes (NP) and focal depth obtained from minimum-misfit point-source solution are given in the header. Slip model is derived on NP1; white star, location of the rupture initiation (initial break) located at a depth of about 18 km (origin of the plot axes). The slip vectors and the distribution of slip magnitudes are also presented. Along-dip distances are shown on the left *y* axis and depth beneath the surface on the right *y* axis. The color scale shows the displacement magnitude in meters. (b) Comparison of the observed (black) and synthetic (red) broadband *P* waveforms used in slip-distribution inversion. Station code and maximum amplitude are shown above the waveforms, station azimuth, and distance below.

for the rake was estimated to be 71° based on our point-source solution. Maximum displacement was found to be ~3.5 m at a depth of about 20 km (Fig. 3). The slip model shows that rupture propagated along the dip direction of the fault. The maximum slip is close to the hypocenter, as expected from the peak in the moment rate function less than 4 s after the origin time of the earthquake. Our preferred finite-fault model has a second area of strong slip to the southwest and shallower than the hypocenter. Other areas of up to 1 m of slip far to the northwest and southwest of the hypocenter are less well constrained. The source time function reveals that the earthquake duration was ~16 s, but the main moment release was in the first 7–8 s. The total moment of the finite-fault model is 5.37×10^{19} N·m. The effective rupture area, stress drop, maximum slip, and average slip were also estimated by using equations of Aki (1972) and Kanamori (1994) to be ~900 km^2, 5 MPa, 3.5 m, and 1.85 m, respectively. The stress drop was estimated with the following equation based on the assumption of a circular crack (Aki, 1972; Kanamori, 1994):

$$\Delta\sigma = \frac{7 \times \pi^{3/2}}{16} \times \frac{M_0}{S^{3/2}}.$$

Average slip is calculated by using the seismic moment equation of Aki (1972); $M_0 = \mu \times A \times D$ for which rigidity μ = 30 GPa (the rigidity of the top 15 km in our velocity model); A, faulting area; D, average displacement. The rupture front is estimated to propagate smoothly along a northeast–southwest direction with a slip-vector of 14° in the up-dip direction after initial downdip propagation from the hypocenter at 18 km depth (see Ⓔ Fig. S8 and Movie S1 [see supplement] for the temporal evolution).

GEODETIC DATA

We analyzed synthetic aperture radar (SAR) data from two satellite systems: the European Space Agency (ESA) Envisat satellite and Italian Space Agency (ASI) COSMO-SkyMed (CSK) constellation. Envisat SAR image pairs that cover the earthquake were available from two descending (satellite moving south and looking west) tracks (see Fig. 1 and Table 3). CSK acquisitions were focused on the city of Van before the earthquake, so the coseismic CSK pair has limited coverage of the area of the mainshock epicenter and aftershocks (Fig. 4) to the north of the city. We performed interferometric SAR (InSAR) analysis on both the Envisat and CSK image pairs, and pixel offset tracking or sub-pixel correlation on the CSK SAR image pair to measure the coseismic deformation. All SAR data was processed from raw signal data using the Jet Propulsion Laboratory-Caltech ROI_pac software (Rosen *et al.*, 2004). For the smaller CSK SAR images, range and azimuth extension (partial focusing) significantly increased the area of the focused images and interferogram (Fig. 4) compared with the standard single-look complex images processed by ASI.

Because of the large strain and strong surface displacement gradients close to the earthquake rupture, phase unwrapping was more challenging in that area. In addition, it probably snowed before the acquisition of the post-earthquake Envisat scene on track D394 (see Fig. 5), so InSAR coherence was low in most of the higher elevations for that pair. We used two iterations of the processing and model inversion to improve the phase unwrapping. First, we unwrapped the standard differential interferograms and derived a simple-fault-model slip inversion with an assumed fault geometry based on the USGS finite-fault model (Hayes, 2011, http://earthquake.usgs.gov/earthquakes/eqinthenews/2011/usb0006bqc/finite_fault.php, last accessed 29 January 2013). We then used the predicted surface displacement field from the preliminary model to subtract the main part of the coseismic deformation from the interferograms, and repeated the phase unwrapping using the Statistical-Cost, Network-Flow Algorithm for Phase Unwrapping (SNAPHU) software (Chen and Zebker, 2002). After unwrapping with the model removed and masking low-coherence areas, we added back the model displacements to make the final interferogram. For the Envisat track D121 interferogram, we also estimated a new effective orbital baseline to remove a long-wavelength ramp, which is probably due to atmospheric water vapor variations, but is similar to orbit error (Fig. 5 shows the corrected interferogram).

The SAR pixel offset tracking (or subpixel correlation) was performed by matching the CSK amplitude images using the ROI_pac ampcor program (Pathier *et al.*, 2006). This involves cross-correlation of 64 by 64 pixel windows from the full-resolution (single-look complex) amplitude images to estimate the offset or distortion of the post-earthquake radar image relative to the pre-earthquake image to a fraction of the pixel size. Measurements are done in the SAR image geometry so they have components in the slant-range and along-track directions. We use the along-track offsets (Fig. 6) to provide an estimate of displacements in the 190° E direction (roughly south). Because of the high spatial resolution of the CSK images (~2 m along track), the pixel offsets can be measured with a precision of

Table 3
SAR Image Pairs Used in Coseismic Analysis

Date 1 (yyyy/mm/dd)	Date 2 (yyyy/mm/dd)	Satellite/Track	Bperp Start	Bperp End	Incidence angle (Center)
2011/10/10	2011/10/26	CSK	−115 m	−116 m	29.8°
2010/11/05	2011/10/31	Envisat/121	153 m	−139 m	41°
2011/07/22	2011/11/19	Envisat/394	−164 m	−262 m	41°

All scenes are from descending tracks (satellite moving southward).

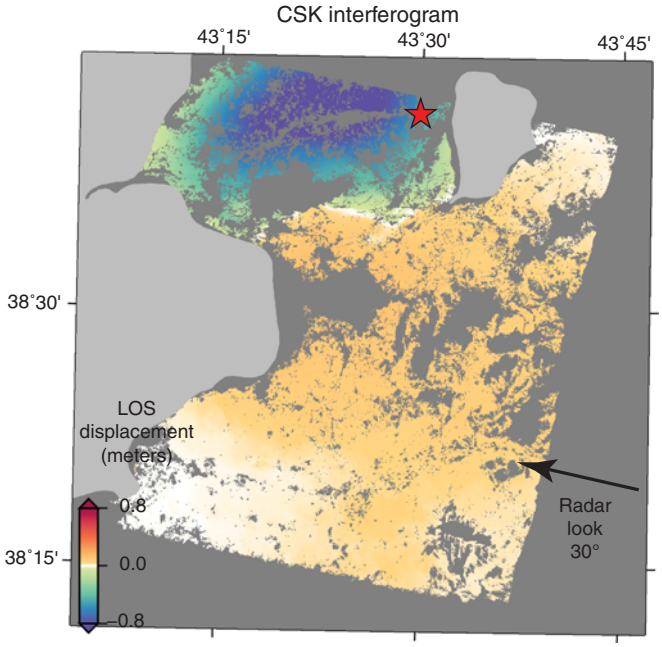

▲ **Figure 4.** CSK interferogram from 10 October 2011 to 26 October 2011, unwrapped phase converted to line-of-sight displacements in meters. Negative displacement means range to satellite decreased as surface moved upward or eastward; red star, epicenter of M_w 7.1 mainshock.

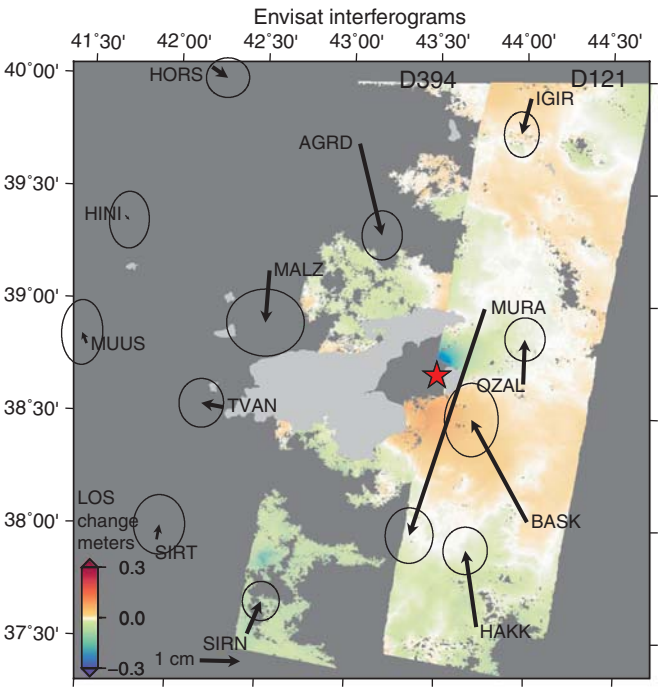

▲ **Figure 5.** Envisat interferograms from both tracks combined (see Table 2 for dates) with GPS coseismic horizontal offsets. Unwrapped phase converted to line-of-sight range change in meters; GPS error ellipses, 95% confidence interval; red star, mainshock epicenter.

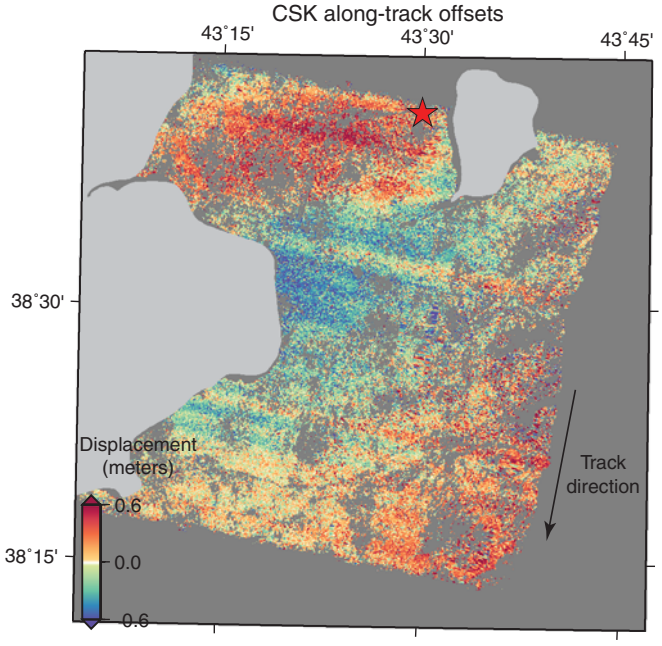

▲ **Figure 6.** CSK pixel tracking offsets in the along-track direction from 10 October 2011 to 26 October 2011. Positive displacements are to the south; red star, epicenter of M_w 7.1 mainshock.

about 10 cm, but various noise effects degrade the accuracy to about 20 cm, so these offset measurements are only useful if the displacements are large. The along-track offsets are only consistent with the north-dipping planes of the point-source focal mechanisms and moment tensors because the surface around the epicenter moved southward.

GPS data from the Continuously Operating Reference Stations (CORS) network called TUSAGA, operated by the Turkish government, were made available online for this earthquake (http://www.hgk.msb.gov.tr/van_depremi_metin.htm, last accessed September 2012). We analyzed the GPS data using JPL's GIPSY-OASIS software and JPL GPS orbit and clock products, applying the single-station bias-fixing strategy described in Bertiger *et al.* (2010). This analysis strategy results in absolute positions in the IGS08 reference frame that have several mm accuracy in the horizontal component and approximately 1 cm accuracy in the vertical component for stations with high-quality data. Coseismic offsets (Fig. 5) were computed by differencing a pre- and post-earthquake position at each site, using approximately two months of data prior to the earthquake and 18 days of data after the earthquake. The average positions were calculated by fitting a linear velocity model to the pre- and post-earthquake position time series, and then using this linear velocity model to estimate the station position on 22 October 2011 (the day before the earthquake) and 24 October 2011 (the day after the earthquake). Because formal errors from the positions are usually an underestimate of the actual accuracy, the errors for the coseismic offsets were calculated by first estimating the root mean square (rms) of the residuals to the linear velocity models to generate pre- and post-earthquake error estimates for the positions in

north, east, and up, and then by applying the standard propagation-of-errors formula to calculate the coseismic offset errors in the individual north, east, and up components.

GEODETIC SOURCE INVERSION

We use the SAR and GPS data described above to constrain a Bayesian inference method with Markov-chain Monte Carlo (MCMC) sampling to resolve the fault rupture location, size, and final slip distribution with posterior probability distribution estimates for the geometric parameters. The Bayesian inference method is based on Fukuda and Johnson (2008). We use a single planar fault embedded in a homogeneous elastic half-space for the earthquake-slip geodetic inversion. We fixed only the depth to the top of the fault at 100 m beneath the surface and allowed the other fault geometry parameters to vary: horizontal location of the top center of the fault, dip, strike, width downdip, and length of the fault. The depth of the top was fixed to avoid trade-offs between the horizontal position and the depth of the top of the model fault. Because we solve for distributed slip at each iteration of the MCMC inversion, the extent of the model fault is not very important as the inversion can put insignificant slip on patches at the edges.

At each step of the Markov-chain sampling, the geometric parameters were changed and then the distribution of slip was inverted using singular-value decomposition (SVD) with Laplacian smoothing regularization imposed on the strike-slip and dip-slip components of slip on each fault patch. Note that the SVD inversion does not include a positivity constraint. The gamma factors controlling the strength of smoothing for the two components and the two weighting factors for the SAR and GPS datasets were also varied at each step of the Markov-chain sampling. After each Markov-chain step, the weighted RMS error of the new fit to the observations is compared with the previous kept fit and the new model is kept if it is better than the previous model or if the exponential of the difference between the previous and current misfits is greater than a random number between zero and one (Fukuda and Johnson, 2008). Note that a new kept model in our MCMC inversion may have slightly worse misfits to the observations than previous kept models because the rms errors are a combination of the observation and model errors, unlike other types of inversions that try to converge on a single best-fit solution. The set of kept solutions after a large number of steps forms an estimate of the posterior probability distribution function for the fault geometric parameters, and the most probable values for each parameter are the values that have the greatest number of kept solutions (Fukuda and Johnson, 2008).

The geodetic MCMC inversion was run using the GPS horizontal and vertical displacements, CSK interferogram and along-track (azimuth) offsets, and two Envisat interferograms from tracks D121 and D394. The geodetic modeling was performed in a local Cartesian coordinate system with the origin at 43.5° E and 38.5° N. The most probable fault geometry had a compact area of high slip that extends approximately 30 km along strike (Fig. 7), with most probable strike and dip of $259 + 2/ - 1°$ and $42.5 + 3/ - 2°$, respectively. Note that the aftershocks from the Bogazici University Kandilli Observatory and Earthquake Research Institute-Ulusal Deprem İzleme Merkezi (National Earthquake Monitoring Centre) (KOERI-UDIM) catalog include many events for which the depth was fixed to 5 km, so those aftershock locations were plotted on Figure 7a but not on Figure 7b. The seismic moment (M_0) calculated from the geodetic slip model is 5.84×10^{19} N·m (M_w 7.13), using a crustal shear modulus of 30 GPa (same modulus as the upper 15 km of the elastic model for our waveform finite-fault inversion). The M_0 would be 8.57×10^{19} N·m (M_w 7.22) with the shear modulus of 44 GPa that was used for the point-source seismic modeling. The estimated posterior distribution functions for all the fault geometrical parameters are shown in Figure 8. Because fault patches around the edges of the model have insignificant slip, the most probable length (48 km) and downdip width (44 km) of the whole modeled fault are not as significant as the area of large fault slip. There is some trade-off between the length and easting of the center of the model fault, but the main slip patch remains in the same horizontal location (Fig. 7) because of the strong constraints of the SAR data. The posterior distribution functions for the weighting and smoothing factors are shown in Figure 9. The posterior distribution functions are somewhat irregular due to nonlinear effects and trade-offs when optimizing the fault geometry, so they are not the same as the often-assumed Gaussian error distributions.

The most probable slip model from the geodetic inversion fits the data well (Fig. 10), with an overall average rms residual of 6 cm. The CSK along-track or azimuth offsets (top row of Fig. 10) have a residual that is close to a planar ramp. This is likely due to a poor estimate of the InSAR baseline effects on the along-track offsets because the earthquake deformation distorts a large portion of the CSK scene. The CSK interferogram (second row) is very well fit by the model prediction, except near the top of the fault where the simple planar fault and large fault patches are not exactly matching the actual fault geometry. The Envisat track D394 interferogram (third row) also has a residual that has a long spatial wavelength that is likely due to water vapor variations or orbit error. The Envisat track D121 interferogram (fourth row) does not have a long-wavelength residual because we estimated and removed an empirical orbit correction (described previously). The GPS displacements (bottom row of Fig. 10) are all fit within the 95% error estimates. Even though the GPS displacements at distances greater than about 100 km are much smaller than their error estimates (see Fig. 5), they are still valuable for constraining the overall moment of the earthquake because they constrain the surface displacements near zero at those locations. The GPS vertical displacements have greater uncertainty so measured vertical displacements far from the fault are probably not due to the main earthquake. The two GPS stations to the east and southeast (OZAL and BASK) have horizontal residuals that are close to the error estimate and both residuals are to the northwest direction. This may indicate that our planar

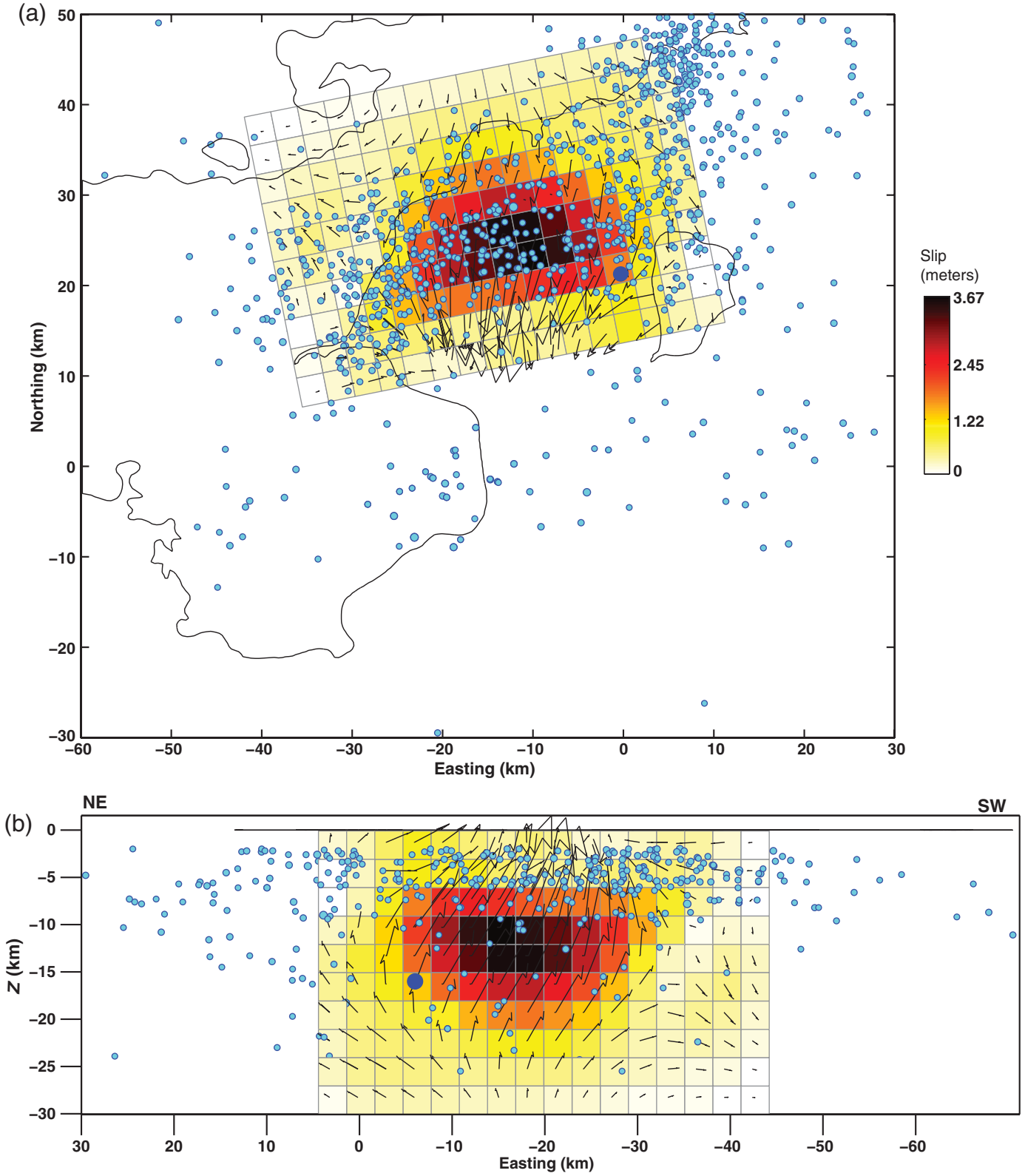

▲ **Figure 7.** Views of estimated most probable fault geometry and slip distribution from geodetic data inversion. Color shows slip magnitude and arrows show direction of motion of hanging wall on each fault patch. Easting and northing are local coordinates relative to latitude 38.5° and longitude 43.5°; large blue circle, mainshock location from the USGS National Earthquake Information Center; small cyan circles, locations of aftershocks with magnitudes greater than 3 from the KOERI catalog (KOERI-UDIM, 2012). (a) Map view of fault patches projected to surface. (b) Fault normal view of hanging wall (looking roughly south) showing fault-slip distribution in cross section with 1:1 vertical scale. Aftershocks with fixed depths have been removed from this view.

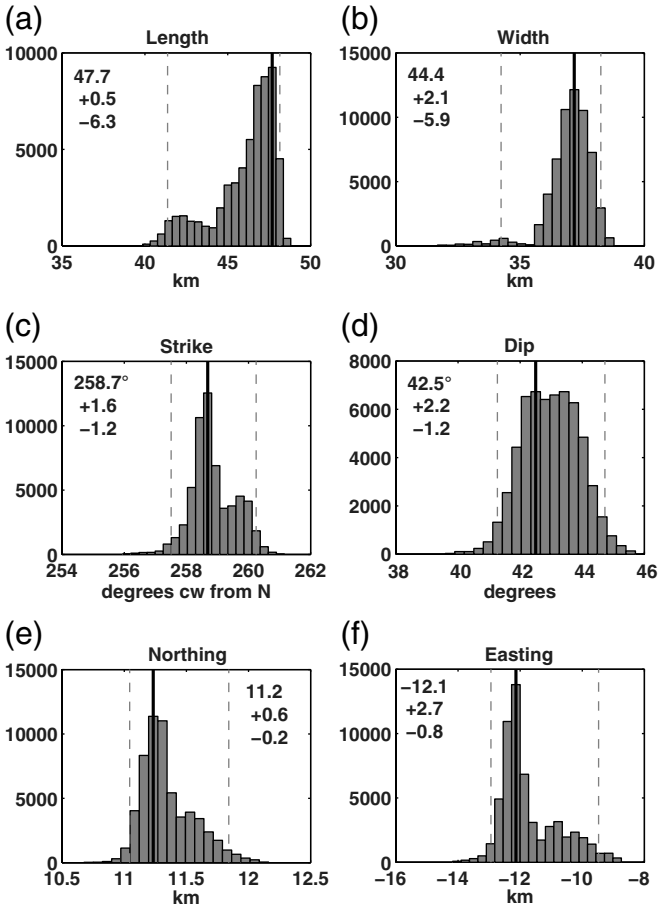

▲ **Figure 8.** Estimated posterior error distributions for the geometrical parameters of the fault from the geodetic data inversion after 60,000 runs; solid lines on histograms, most probable solution; dashed lines, 95% probability limits estimated from histogram.

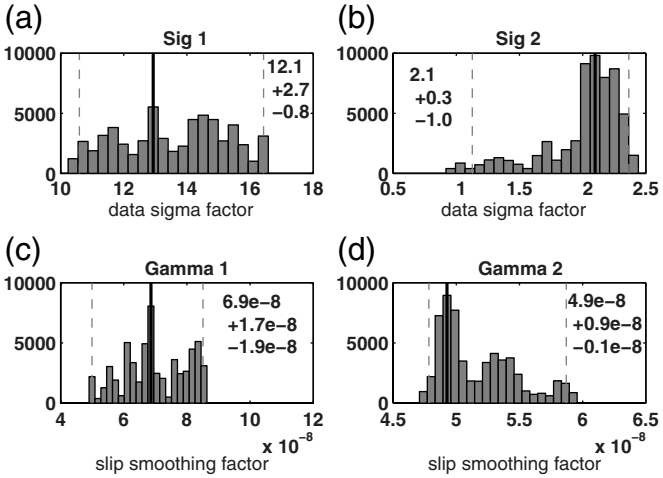

▲ **Figure 9.** Estimated posterior distribution functions for weighting and smoothing parameters from geodetic inversion after 60,000 runs. Panels (a) and (b) show dataset weighting factors for SAR and GPS datasets, respectively. Panels (c) and (d) show smoothing parameters for dip-slip and strike-slip components of fault slip, respectively; solid lines on histograms, most probable solution; dashed lines, 95% probability limits estimated from histogram.

fault model or the homogeneous elastic structure is too simple. Elliott *et al.* (2013) preferred a fault model with two faults that have different dips along strike, which we did not study.

Our most probable slip model from the geodetic inversion has peak slip slightly less than 4 m at a depth close to 12 km and the area of major slip extended about 30 km along strike (Fig. 7). Slip decreases sharply at a depth of about 6–8 km, with less than a meter of slip above that depth. The surface geodetic data has less resolution at depth, so we cannot determine the bottom depth of the coseismic slip precisely, but it is likely that the slip extended to at least 22 and perhaps 25 km depth. As mentioned above, we did not apply any constraint on the rake or direction of slip, so some patches with small magnitude in the lower southwest have slip, which would correspond to normal dip-slip. This is probably an artifact of the inversion because that part of the model fault is beneath Lake Van and therefore has no SAR data over it to constrain the slip (Fig. 7a). Our geodetic finite-fault model has only a single main slip patch, but our body-wave finite-fault model has two slip patches, which could be similar to the two slip patches of the Elliott *et al.* (2013) preferred geodetic model. Different amounts of smoothing strongly affect the roughness of the inversion results, but our Bayesian geodetic inversion found that a single slip patch was most likely given the *a priori* assumption of a single fault plane.

DISCUSSION AND CONCLUSIONS

The strike and dip estimates of the preferred body waveform point-source solution, which was used for the waveform finite-fault solution, and the geodetic inversion solution agree within the estimated errors. The horizontal location of the point source or finite-fault fault plane is not estimated in our body waveform inversions, so the location is fixed to the USGS-NEIC hypocenter location. The InSAR and pixel-tracking measurements from the CSK data provide strong constraints on the strike and dip of the main rupture and the location of the fault plane (see Fig. 8). The waveform finite-fault and geodetic models both have major slip extending about 30 km along strike and from depths of about 25–8 km beneath the surface. The peak slip in the geodetic inversion (~12 km) is shallower than the peak in the waveform finite-fault inversion (~20 km). Joint inversions of geodetic and teleseismic waveform data for other large earthquakes (Pritchard and Fielding, 2008; Hayes *et al.*, 2010; Sladen *et al.*, 2010; Wei *et al.*, 2011) showed that the depth of slip is usually constrained better by the geodetic data at least for depths shallower than about 20 km.

The total seismic moment for the two finite-fault inversion methods we used are similar (within 14%, 5.37×10^{19} N·m versus 5.84×10^{19} N·m), but the geodetic moment is larger, perhaps because it includes days to weeks of postseismic deformation (our GPS offsets are estimated for one day after the earthquake, the CSK scene that we use was acquired three days

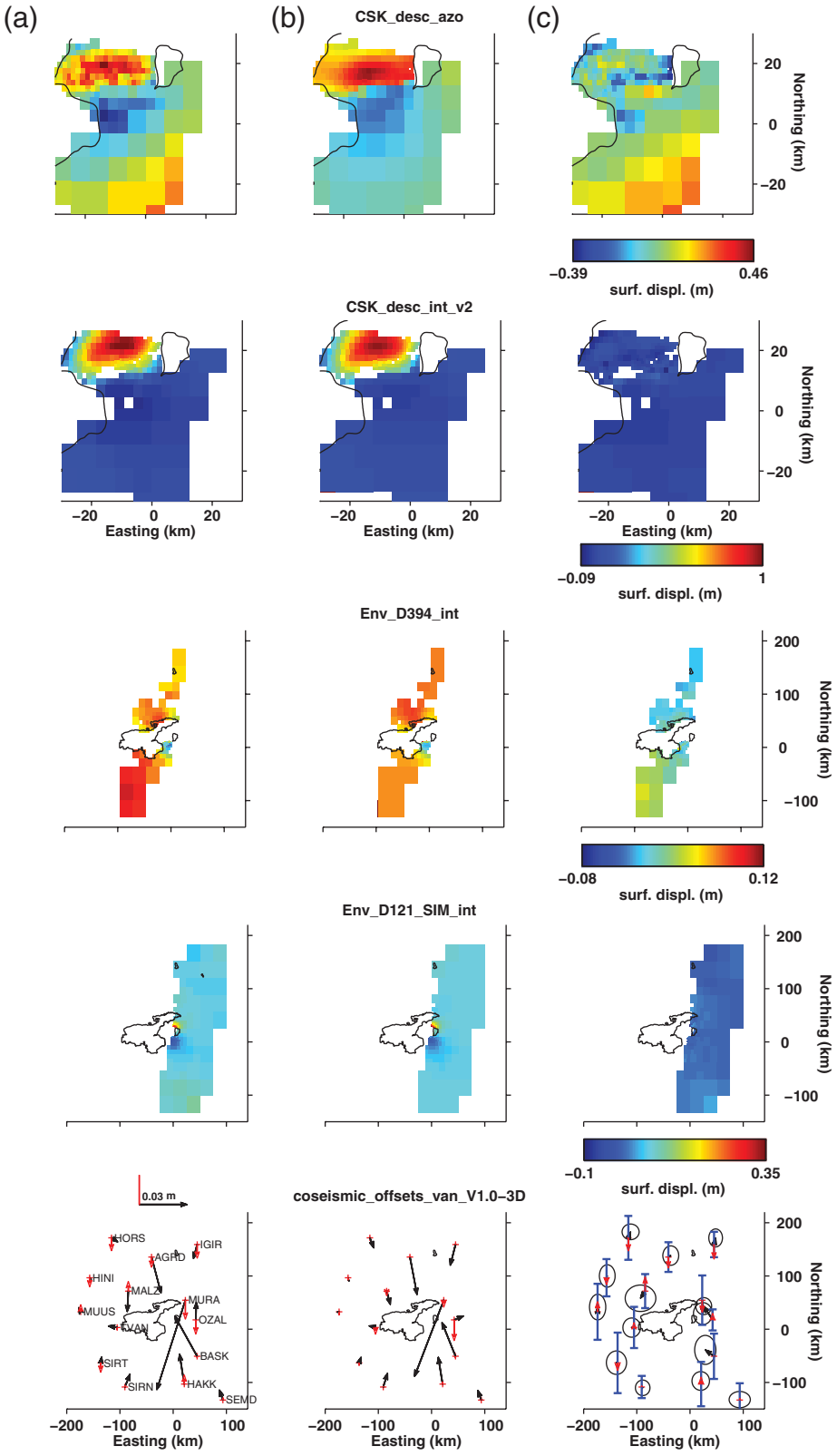

▲ **Figure 10.** Geodetic data inputs, model predictions, and residuals for most probable model from geodetic inversion. (a) Sampled SAR (CSK: COSMO-SkyMed and Env: Envisat) interferograms and along-track offsets along with GPS coseismic displacements; black vectors, horizontal displacements; red vectors, vertical displacements. (b) Predictions from most probable model. (c) Residual of data minus model; black, GPS error ellipses at 95% confidence for horizontal displacements shown on residual plot; blue bars, (2σ) vertical errors. Note that the map scale for CSK data (top two rows) is different from the rest of the rows.

after the earthquake, and the Envisat scenes were acquired later; see Table 2). The moment of our preferred point source model is considerably smaller than the two finite-fault models (about 3.4×10^{19} N·m) if converted to the shear modulus of 30 GPa that we used for our geodetic moment calculation (the shear modulus for our teleseismic finite fault model is 30 GPa at depths 0–15 km and 40 GPa 15–33 km, so approximately the same). A body-wave study that explored the dependence of the seismic moment on the centroid depth for the Van mainshock found that the moment increases drastically if the centroid is fixed to shallower depths (Elliott *et al.*, 2013), with the moment close to 5×10^{19} N·m for a centroid depth of about 12 km (at the peak of our geodetic slip model). Our geodetic estimate of the seismic moment (5.84×10^{19} N·m for shear modulus 30 GPa or 6.23×10^{19} N·m for modulus 32 GPa often used) is close to the Global Centroid Moment Tensor M_0 of 6.40×10^{19} N·m (from http://globalcmt.org) and is larger than M_0 5.53×10^{19} N·m of the finite-fault model from bodywave inversion of Irmak *et al.* (2013). It is possible that some energy was released in slower slip, which was not measured by the teleseismic body waves.

Our analysis indicates that the 2011 mainshock primarily ruptured the middle crust and the shallowest part had much less slip. The slip was primarily thrust with minor strike-slip motion. The 2011 Van mainshock earthquake is similar to other large events on blind thrust faults, including the 1983 Coalinga, California, earthquake (Fielding *et al.*, 1984), 1989 Loma Prieta, California, earthquake (Zhang and Lay, 1990), and 1994 Northridge, California, earthquake (Jones *et al.*, 1994). Field geologists mapped some surface ruptures with lengths up to a km or two north of Van with tens of cm of offset (Doğan and Karakaş, 2013; Elliott *et al.*, 2013; Irmak *et al.*, 2013), but it is not clear whether these fault ruptures are directly connected to the main rupture at depth or are separate faults. The shallow fault slip observed in the field may be triggered slip from the dynamic and static stress changes of the mainshock. A CSK interferogram from four hours to three days after the mainshock shows clear shallow afterslip (Elliott *et al.*, 2013). CSK and TerraSAR-X interferograms covering longer time intervals after the 23 October 2011 mainshock show that several faults slipped for days and weeks after the **M** 7.1 earthquake (unpublished manuscript). It is clear that the area of major slip stops at about 6–8 km beneath the surface (Fig. 7), so shallower thrust faults in the crust now have increased stress, which could lead to future large earthquakes in the next years or decades, similar to the M_w 6.6 1998 Fandoqa earthquake in Iran that ruptured 17 years after two large **M** 7 deeper events in 1981 (Berberian *et al.*, 2001). We note that such triggering does not always occur: the 1983 Coalinga, 1989 Loma Prieta, and 1994 Northridge events have not yet had shallow $\mathbf{M} > 6$ earthquakes above them. The Coalinga earthquake was followed by $\mathbf{M} > 6$ earthquakes on adjacent structures (Ekström *et al.*, 1992).

The 2011 Van earthquake main rupture probably reached depths of about 25 km (Figs. 6 and 7). This is slightly more than half of the 43 km crustal thickness (Gök *et al.*, 2011; Vanacore *et al.*, 2013) and indicates that the middle crust in this part of the Turkish–Iranian Plateau is strong enough to rupture in large earthquakes despite extensive volcanism that has heated the crust and an unusually hot uppermost mantle. This makes the Turkish–Iranian Plateau distinctive from the highly extended Basin and Range province or the much thicker Tibetan Plateau that have earthquakes only down to about 15 km (e.g., Pancha *et al.*, 2006; Elliott *et al.*, 2010). It is also clear that the Turkish–Iranian Plateau is still undergoing north–south shortening consistent with the GPS measurements (Reilinger *et al.*, 2006) with some of the strain absorbed by roughly east–west-trending thrust faults, in addition to the previously mapped active strike-slip structures (Copley and Jackson, 2006; Tan and Taymaz, 2006).

ACKNOWLEDGMENTS

We thank an anonymous reviewer for detailed comments on earlier versions of our manuscript that helped us to improve it. We thank M. Barazangi, Z. Liu, S. Akçiz, E. Hauksson, J. Elliott, and K. Hudnut for discussions. We thank S. Ergintav for helping to arrange the sharing of the GPS data on the Geohazards Supersite. We thank B. Doğan for sending preprints of papers in advance of publication. We would like to thank İstanbul Technical University Research Fund (İTÜ-BAP), Turkish National Scientific, Technological Foundation (TÜBİTAK), Turkish Academy of Sciences (TÜBA) in the framework for Young Scientist Award Program (TT-TÜBA-GEBIP 2001-2-17), and Alexander von Humboldt-Stiftung (AvH) for their support. Generic Mapping Tools (GMT; Wessel and Smith, 1998) and SAC2000 software packages (Goldstein *et al.*, 2003) were used to prepare figures and to process conventional earthquake data, respectively. We are thankful to Yeşim Çubuk for her help in generating Figure 1 and Table 1. The teleseismic body waves used in this study are from the International Federation of Digital Seismograph Networks (FDSN), the Global Digital Seismograph Network (GDSN) stations and archived at the IRIS-DMC. COSMO-SkyMed (CSK) original data are copyright 2011 by the Italian Space Agency and was provided under CSK AO PI project 2271. Envisat original data are copyright 2010–2011 by the European Space Agency and was delivered under the Group on Earth Observation (GEO) Geohazards Supersite program. Part of this research was sponsored by the NASA Earth Surface and Interior focus area and performed at the Jet Propulsion Laboratory, California Institute of Technology.

REFERENCES

Aki, K. (1972). Earthquake mechanism, *Tectonophysics* **13,** 423–446.

Albini, P., M. B. Demircioglu, M. Locati, A. Rovida, K. Sesetyan, M. Stucchi, and D. Viganò (2012). In search of the predecessors of the 2011 Van (Turkey) earthquake, *Seismol. Res. Lett.* **83,** 855–862.

Al-Damegh, K., E. Sandvol, A. Al-Lazki, and M. Barazangi (2004). Regional seismic wave propagation (Lg and Sn) and Pn attenuation in the Arabian Plate and surrounding regions, *Geophys. J. Int.* **157,** 775–795.

Ambraseys, N. N., and J. A. Jackson (1998). Faulting associated with historical and recent earthquakes in the eastern Mediterranean region, *Geophys. J. Int.* **133,** 390–406.

Bakırcı, T., K. Yoshizawa, and M. F. Özer (2012). Three-dimensional S-wave structure of the upper mantle beneath Turkey from surface wave tomography, *Geophys. J. Int.* **190,** 1058–1076.

Barazangi, M., E. Sandvol, and D. Seber (2006). Structure and tectonic evolution of the Anatolian plateau in eastern Turkey, in *Postcollisional Tectonics and Magmatism in the Mediterranean Region and Asia*, Y. Dilek and S. Pavlides (Editors), Geol. Soc. Am., Boulder, 463–473.

Berberian, M., J. A. Jackson, E. J. Fielding, B. E. Parsons, K. Priestley, M. Qorashi, M. Talebian, R. Walker, T. J. Wright, and C. Baker (2001). The 1998 March 14 Fandoqa earthquake (M_w 6.6) in Kerman province, southeast Iran: Re-rupture of the 1981 Sirch earthquake fault, triggering of slip on adjacent thrusts and the active tectonics of the Gowk fault zone, *Geophys. J. Int.* **146,** 371–398.

Bertiger, W., S. D. Desai, B. Haines, N. Harvey, A. W. Moore, S. Owen, and J. P. Weiss (2010). Single receiver phase ambiguity resolution with GPS data, *J. Geod.* **84,** 327–337.

Chen, C. W., and H. A. Zebker (2002). Phase unwrapping for large SAR interferograms: Statistical segmentation and generalized network models, *IEEE Trans. Geosci. Remote Sens.* **40,** 1709–1719.

Christensen, D. H., and L. J. Ruff (1985). Analysis of the trade-off between hypocentral depth and source time function, *Bull. Seismol. Soc. Am.* **75,** 1637–1656.

Copley, A., and J. Jackson (2006). Active tectonics of the Turkish-Iranian Plateau, *Tectonics* **25,** TC6006.

Doğan, B., and A. Karakaş (2013). Geometry of co-seismic surface ruptures and tectonic meaning of the 23 October 2011 M_w 7.1 Van earthquake (East Anatolian Region, Turkey), *J. Struct. Geol.* **46,** 99–114.

Dziewonski, A. M., and D. L. Anderson (1981). Preliminary reference earth model, *Phys. Earth Planet. In.* **25,** 297–356.

Ekström, G., R. S. Stein, J. P. Eaton, and D. Eberhart-Phillips (1992). Seismicity and geometry of a 110-km-long blind thrust-fault. 1. The 1985 Kettleman Hills, California, earthquake, *J. Geophys. Res.* **97,** 4843–4864.

Elliott, J. R., A. C. Copley, R. Holley, K. Scharer, and B. Parsons (2013). The 2011 M_w 7.1 Van (Eastern Turkey) earthquake, *J. Geophys. Res.* Solid Earth, **118,** doi: 10.1002/jgrb.50117.

Elliott, J. R., R. J. Walters, P. C. England, J. A. Jackson, Z. Li, and B. Parsons (2010). Extension on the Tibetan plateau: Recent normal faulting measured by InSAR and body wave seismology, *Geophys. J. Int.* **183,** 503–535.

Ergin, K., U. Güçlü, and Z. Uz (1967). *Earthquake Catalog of Turkey and Surroundings*, Faculty of Mines Printing House, Istanbul Technical University, Istanbul, Turkey.

Fielding, E. J., M. Barazangi, L. Brown, J. Oliver, and S. Kaufman (1984). COCORP seismic profiles near Coalinga, California: Subsurface structure of the western Great Valley, *Geology* **12,** 268–273.

Fredrich, J., R. McCaffrey, and D. Denham (1988). Source parameters of seven large Australian earthquakes determined by body waveform inversion, *Geophys. J.* **95,** 1–13.

Fukuda, J., and K. M. Johnson (2008). A fully Bayesian inversion for spatial distribution of fault slip with objective smoothing, *Bull. Seismol. Soc. Am.* **98,** 1128–1146.

Futterman, W. I. (1962). Dispersive body waves, *J. Geophys. Res.* **67,** 5279–5291.

Gök, R., R. J. Mellors, E. Sandvol, M. Pasyanos, T. Hauk, R. Takedatsu, G. Yetirmishli, U. Teoman, N. Turkelli, T. Godoladze, and Z. Javakishvirli (2011). Lithospheric velocity structure of the Anatolian plateau-Caucasus-Caspian region, *J. Geophys. Res.* **116,** B05303.

Gök, R., E. Sandvol, N. Türkelli, D. Seber, and M. Barazangi (2003). Sn attenuation in the Anatolian and Iranian plateau and surrounding regions, *Geophys. Res. Lett.* **30,** 8042.

Goldstein, P., D. Dodge, M. Firpo, and L. Minner (2003). SAC2000: Signal processing and analysis tools for seismologists and engineers, in *The IASPEI International Handbook of Earthquake and Engineering Seismology*, W. H. K. Lee, H. Kanamori, P. C. Jennings, and C. Kisslinger (Editors), Vol. 81B, Chapter 85.5, Academic Press, London, 1613–1620, ISBN: 0-12-440-658-0.

Hartzell, S. H., and T. H. Heaton (1983). Inversion of strong ground motion and teleseismic waveform data for the fault rupture history of the 1979 Imperial Valley, California, earthquake, *Bull. Seismol. Soc. Am.* **73,** 1553–1583.

Hayes, G. P., R. W. Briggs, A. Sladen, E. J. Fielding, C. Prentice, K. Hudnut, P. Mann, F. W. Taylor, A. J. Crone, R. Gold, T. Ito, and M. Simons (2010). Complex rupture during the 12 January 2010 Haiti earthquake, *Nature Geosci.* **3,** 800–805, doi: 10.1038/ngeo977.

Irmak, T. S., B. Doğan, and A. Karakaş (2012). Source mechanism of the 23 October 2011 Van (Turkey) earthquake ($M_w = 7.1$) and aftershocks with its tectonic implications, *Earth Planets Space* **64,** 991–1003, doi: 10.5047/eps.2012.05.002.

Jackson, J., and D. McKenzie (1984). Active tectonics of the Alpine–Himalayan Belt between western Turkey and Pakistan, *Geophys. J. Roy. Astron. Soc.* **77,** 185–264.

Jackson, J., and D. McKenzie (1988). The relationship between plate motions and seismic moment tensors, and the rates of active deformation in the Mediterranean and Middle-East, *Geophys. J.* **93,** 45–73.

Jackson, J., K. Priestley, M. Allen, and M. Berberian (2002). Active tectonics of the South Caspian basin, *Geophys. J. Int.* **148,** 214–245.

Jeffreys, H., and K. E. Bullen (1940, 1958). *Seismological Tables*, Brit. Assoc. for the Advanc. of Science, Gray-Milne Trust, London.

Jones, L., K. Aki, D. Boore, M Celebi, A. Donnellan, J. Hall, R. Harris, E. Hauksson, T. Heaton, S. Hough, K. Hudnut, K. Hutton, M. Johnston, W. Joyner, H. Kanamori, G. Marshall, A. Michael, J. Mori, M. Murray, D. Ponti, P. Reasenberg, D. Schwartz, L. Seeber, A. Shakal, R. Simpson, H. Thio, J. Tinsley, M. Todorovska, M. Trifunac, D. Wald, and M. L. Zoback (1994). The magnitude-6.7 Northridge, California, earthquake of 17-January-1994, *Science* **266,** 389–397.

Kanamori, H. (1994). Mechanics of earthquakes, *Annu. Rev. Earth Planet. Sci.* **22,** 207–237.

Kikuchi, M., and H. Kanamori (1991). Inversion of complex body waves-III, *Bull. Seismol. Soc. Am.* **81,** 2335–2350.

Koçyiğit, A., A. Yılmaz, S. Adamia, and S. Kuloshvili (2001). Neotectonics of East Anatolian Plateau (Turkey) and Lesser Caucasus: Implication for transition from thrusting to strike-slip faulting, *Geodinamica Acta* **14,** 177–195.

KOERI-UDIM (2012). *Historical Earthquakes Catalog*, Boğaziçi University, Kandilli Observatory and Earthquake Research Institute, National Earthquake Monitoring Centre, Istanbul, Turkey.

Maggi, A., and K. Priestley (2005). Surface waveform tomography of the Turkish–Iranian plateau, *Geophys. J. Int.* **160,** 1068–1080.

McCaffrey, R., P. Zwick, and G. A. Abers (1991). *SYN4 Program*, IASPEI Software Library 3, 81–166.

Nabelek, J. (1984). Determination of earthquake source parameters from inversion of body waves, *Ph.D. Thesis*, Mass. Inst. of Tech., Cambridge, Massachusetts, USA.

Nabelek, J. (1985). Geometry and mechanism of faulting of the 1980 El-Asnam, Algeria, earthquake from inversion of teleseismic body waves and comparison with field observations, *J. Geophys. Res.* **90,** 2713–2728.

Örgülü, G., M. Aktar, N. Türkelli, E. Sandvol, and M. Barazangi (2003). Contribution to the seismotectonics of Eastern Turkey from moderate and small size events, *Geophys. Res. Lett.* **30,** 8040.

Pancha, A., J. G. Anderson, and C. Kreemer (2006). Comparison of seismic and geodetic scalar moment rates across the Basin and Range province, *Bull. Seismol. Soc. Am.* **96,** 11–32.

Pathier, E., E. J. Fielding, T. J. Wright, R. Walker, B. E. Parsons, and S. Hensley (2006). Displacement field and slip distribution of the 2005 Kashmir earthquake from SAR imagery, *Geophys. Res. Lett.* **33,** L20310, doi: 10.1029/2006GL027193.

Podgorski, J., E. H. Hearn, S. McClusky, R. Reilinger, T. Taymaz, O. Tan, M. Prilepin, T. Guseva, and M. Nadariya (2007). Postseismic deformation following the 1991 Racha, Georgia, earthquake, *Geophys. Res. Lett.* **34,** L04310.

Pritchard, M. E., and E. J. Fielding (2008). A study of the 2006 and 2007 earthquake sequence of Pisco, Peru, with InSAR and teleseismic data, *Geophys. Res. Lett.* **35,** L09308, doi: 10.1029/2008GL033374.

Reilinger, R., S. McClusky, P. Vernant, S. Lawrence, S. Ergintav, R. Cakmak, H. Ozener, F. Kadirov, I. Guliev, R. Stepanyan, M. Nadariya, G. Hahubia, S. Mahmoud, K. Sakr, A. ArRajehi, D. Paradissis, A. Al-Aydrus, M. Prilepin, T Guseva, E. Evren, A. Dmitrotsa, S. V. Filikov, F. Gomez, R. Al-Ghazzi, and G. Karam (2006). GPS constraints on continental deformation in the Africa-Arabia-Eurasia continental collision zone and implications for the dynamics of plate interactions, *J. Geophys. Res.* **111,** B05411, doi: 10.1029/2005JB004051.

Rosen, P. A., S. Hensley, G. Peltzer, and M. Simons (2004). Updated repeat orbit interferometry package released, *EOS Trans. AGU* **85,** 47.

Şengör, A. M. C., S. Özeren, T. Genç, and E. Zor (2003). East Anatolian high plateau as a mantle-supported, north-south shortened domal structure, *Geophys. Res. Lett.* **30,** 8045.

Sladen, A., H. Tavera, M. Simons, J.-P. Avouac, A. O. Konca, H. Perfettini, L. Audin, E. J. Fielding, F. Ortega, and R. Cavagnoud (2010). Source model of the 2007 M_w 8.0 Pisco, Peru earthquake—Implications for seismogenic behavior or subduction megathrusts, *J. Geophys. Res.* **115,** B02405, doi: 10.1029/2009JB006429.

Tan, O., and T. Taymaz (2006). Active tectonics of the Caucasus: Earthquake source mechanisms and rupture histories obtained from inversion of teleseismic body waveforms, *Spec. Pap. Geol. Soc. Am.* **409,** 531–578.

Taymaz, T. (1993). The source parameters of the Çubukdağ (W Turkey) earthquake of 1986 October 11, *Geophys. J. Int.* **113,** 260–267.

Taymaz, T. (1996). *Active Tectonics of the East Anatolia: Source Parameters of Destructive Earthquakes and Seismotectonic Setting*, Turkish National Science Foundation (TÜBİTAK), Ankara, Turkey.

Taymaz, T., and S. Price (1992). The 1971 May 12 Burdur earthquake sequence, SW Turkey: A synthesis of seismological and geological observations, *Geophys. J. Int.* **108,** 589–603.

Taymaz, T., H. Eyidogğan, and J. Jackson (1991). Source parameters of large earthquakes in the East Anatolian Fault Zone (Turkey), *Geophys. J. Int.* **106,** 537–550.

Taymaz, T., T. J. Wright, S. Yolsal, O. Tan, E. J. Fielding, and G. Seyitoğlu (2007). Source characteristics of the 6 June 2000 Orta-Çankırı (central Turkey) earthquake: A synthesis of seismological, geological and geodetic (InSAR) observations, and internal deformation of the Anatolian plate, in *The Geodynamics of the Aegean and Anatolia*, T. Taymaz, Y. Yılmaz, and Y. Dilek (Editors), Geological Society, London, 259–290.

Vanacore, E. A., T. Taymaz, and E. Saygin (2013). Moho structure of the Anatolian Plate from receiver function analysis, *Geophys. J. Int.* **193,** no. 1, 329–337, doi: 10.1093/gji/ggs1107.

Wagner, G. S., and C. A. Langston (1989). Some pitfalls and trade-offs in source parameter determination using body wave modeling and inversion, *Tectonophysics* **166,** 101–114.

Wei, S., E. J. Fielding, S. Leprince, A. Sladen, J.- P. Avouac, D. V. Helmberger, E. Hauksson, R. Chu, M. Simons, K. W. Hudnut, T. Herring, and R. W. Briggs (2011). Superficial simplicity of the 2010 El Mayor–Cucapah earthquake of Baja California in Mexico, *Nature Geosci.* **4,** 615–618.

Wessel, P., and W. H. F. Smith (1998). New, improved version of the Generic Mapping Tools released, *EOS Trans. AGU* **79,** 579.

Yagi, Y., and M. Kikuchi (2000). Source rupture process of the Kocaeli, Turkey, earthquake of August 17, 1999, obtained by joint inversion of near-field data and teleseismic data, *Geophys. Res. Lett.* **27,** 1969–1972.

Yagi, Y., A. Nakao, and A. Kasahara (2012). Smooth and rapid slip near the Japan Trench during the 2011 Tohoku-oki earthquake revealed by a hybrid back-projection method, *Earth Planet. Sci. Lett.* **355,** 94–101.

Yagi, Y., N. Nishimura, and A. Kasahara (2012). Source process of the 12 May 2008 Wenchuan, China, earthquake determined by waveform inversion of teleseismic body waves with a data covariance matrix, *Earth Planets Space* **64,** E13–E16.

Yolsal-Çevikbilen, S., and T. Taymaz (2012). Earthquake source parameters along the Hellenic subduction zone and numerical simulations of historical tsunamis in the Eastern Mediterranean, *Tectonophysics* **536–537,** 61–100.

Yolsal-Çevikbilen, S., C. B. Biryol, S. Beck, G. Zandt, T. Taymaz, H. E. Adıyaman, and A. A. Özacar (2012). 3-D crustal structure along the North Anatolian fault zone in north-central Anatolia revealed by local earthquake tomography, *Geophys. J. Int.* **188,** 819–849.

Yoshida, S. (1992). Wave-form inversion for rupture process using a nonflat sea-floor model—Application to 1986 Andreanof Islands and 1985 Chile earthquakes, *Tectonophysics* **211,** 45–59.

Yoshida, S., K. Koketsu, B. Shibazaki, T. Sagiya, T. Kato, and Y. Yoshida (1996). Joint inversion of near- and far-field waveforms and geodetic data for the rupture process of the 1995 Kobe earthquake, *J. Phys. Earth* **44,** 437–454.

Zhang, J., and T. Lay (1990). Source parameters of the 1989 Loma Prieta earthquake determined from long-period Rayleigh waves, *Geophys. Res. Lett.* **17,** 1195–1198.

Zor, E., E. Sandvol, C. Gürbüz, N. Türkelli, D. Seber, and M. Barazangi (2003). The crustal structure of the East Anatolian plateau (Turkey) from receiver functions, *Geophys. Res. Lett.* **30,** 8044.

Zwick, P., R. McCaffrey, and G. A. Abers (1994). *MT5 program*, IASPEI Software Library 4.

Eric J. Fielding
Paul R. Lundgren
Susan E. Owen
Jet Propulsion Laboratory
California Institute of Technologys
4800 Oak Grove Drive
MS 300-233
Pasadena, California 91109 U.S.A.

Tuncay Taymaz
Seda Yolsal-Çevikbilen
Department of Geophysical Engineering
The Faculty of Mines
Istanbul Technical University
Maslak-34469, Istanbul, Turkey